nanomaterials

Article

Constructing Sheet-On-Sheet Structured Graphitic Carbon Nitride/Reduced Graphene Oxide/Layered MnO_2 Ternary Nanocomposite with Outstanding Catalytic Properties on Thermal Decomposition of Ammonium Perchlorate

Jianhua Xu [1,2,†], Dongnan Li [1,†], Yu Chen [3,†], Linghua Tan [1,*], Bo Kou [3], Fushun Wan [2], Wei Jiang [1] and Fengsheng Li [1]

[1] National Special Superfine Power Engineering Research Center, Nanjing University of Science and Technology, Nanjing 210094, China; xujianhua931118@163.com (J.X.); joshldn@163.com (D.L.); climentjw@126.com (W.J.); lfs_njust@126.com (F.L.)
[2] School of Chemical Engineering, Nanjing University of Science and Technology, Nanjing 210094, China; wanfushun0808@163.com
[3] Jiangsu Key Laboratory of Advanced Structural Materials and Application Technology, School of Materials Engineering, Nanjing Institute of Technology, Nanjing 211167, China; cy_5432@163.com (Y.C.); koutianbo@hotmail.com (B.K.)
* Correspondence: tanlh@njust.edu.cn; Tel.: +86-25-8431-5042
† These author contributed equally to this work.

Received: 27 October 2017; Accepted: 9 December 2017; Published: 15 December 2017

Abstract: We unprecedentedly report that layered MnO_2 nanosheets were in situ formed onto the surface of covalently bonded graphitic carbon nitride/reduced graphene oxide nanocomposite (g-C_3N_4/rGO), forming sheet-on-sheet structured two dimension (2D) graphitic carbon nitride/reduced graphene oxide/layered MnO_2 ternary nanocomposite (g-C_3N_4/rGO/MnO_2) with outstanding catalytic properties on thermal decomposition of ammonium perchlorate (AP). The covalently bonded g-C_3N_4/rGO was firstly prepared by the calcination of graphene oxide-guanidine hydrochloride precursor (GO-GndCl), following by its dispersion into the $KMnO_4$ aqueous solution to construct the g-C_3N_4/rGO/MnO_2 ternary nanocomposite. FT-IR, XRD, Raman as well as the XPS results clearly demonstrated the chemical interaction between g-C_3N_4, rGO and MnO_2. TEM and element mapping indicated that layered g-C_3N_4/rGO was covered with thin MnO_2 nanosheets. Furthermore, the obtained g-C_3N_4/rGO/MnO_2 nanocomposite exhibited promising catalytic capacity on thermal decomposition of AP. Upon addition of 2 wt % g-C_3N_4/rGO/MnO_2 ternary nanocomposite as catalyst, the thermal decomposition temperature of AP was largely decreased up by 142.5 °C, which was higher than that of pure g-C_3N_4, g-C_3N_4/rGO and MnO_2, respectively, demonstrating the synergistic catalysis of the as-prepared nanocomposite.

Keywords: g-C_3N_4/rGO/MnO_2; sheet-on-sheet; covalent coupling; in situ formation; synergistic effect

1. Introduction

Recently, two-dimensional (2D) nanosheets have drawn increasing attention due to their special optical and electronic properties, as 2D nanosheets often show outstanding performance in catalysis [1], sensing [2], nanoelectronic devices [3] and so on. Among all the 2D materials, graphene is particularly attractive owning to its excellent thermal and chemical stability, large surface area and good electronic conductivity [4,5]. As an important derivative of graphene, graphene oxide (GO), which possesses many oxygen-containing functional groups on its basal planes, regarded as potential reactive sites for constructing 2D functional nanocomposite [6]. The prepared layered composite often has excellent properties owning to the interaction between the individual components. For example, by combining the respective advantages of SnS_2 nanosheet (large interlayer spacing benefiting Na^+ intercalation and diffusion) and reduced graphene oxide (rGO) (highly conductive network benefiting conduction of electron), the SnS_2-rGO layered nanocomposite exhibited excellent electrochemical performance when was used as the anode of sodium-ion batteries [7]. Besides, due to intimate contact between WS_2 nanosheet and rGO support, layered WS_2/rGO nanocomposite synthesized via the hydrothermal reaction showed promising catalytic capacity for hydrogen evolution reaction [8]. Thus, it is of great value for constructing GO-based 2D nanomaterials.

Among various layered materials, graphitic carbon nitride (g-C_3N_4) has similar carbon network and sp^2 conjugated π structure compared to GO [9], which is considered as the most compatible material to couple with GO. In recent years, constructing of g-C_3N_4/GO or g-C_3N_4/rGO has been intensely studied. However, few of them focused on the design of covalently linked binary g-C_3N_4/GO or g-C_3N_4/rGO nanocomposite [10,11]. If g-C_3N_4 is covalently coupled with graphene sheets, the prepared composite would possess a very stable structure with excellent catalytic ability via the joint interaction between the individual nanosheets [12]. For example, Fu and his coworkers used an in situ synthetic approach to create a cross-linked g-C_3N_4/rGO composites that can be utilized as the anode of lithium-ion batteries with high, stable and reversible capacity [13]. Ong et al. [14] demonstrated that the sandwich-like graphene-g-C_3N_4 hybrid linked by C–O–C bond showed high visible-light photoactivity towards CO_2 reduction.

Coupling g-C_3N_4/rGO with another 2D materials to construct functional sheet-on-sheet structured ternary nanocomposite attracts substantial research efforts, which was motivated by the desire to combine the properties of each individual nanosheets [15]. Few-layered MnO_2 nanosheet is known as a promising 2D material due to its potential application in many fields, such as supercapacitors [16], selective detection [17], tumor cell imaging [18], fluorescence sensor [19] and photocatalyst [20]. Such wide application made the preparation of MnO_2 nanosheet draw great attention. Thus, it is of great significance to construct 2D g-C_3N_4/rGO/MnO_2 ternary nanocomposite.

Herein, we present the construction and characterization of sheet-on-sheet structured graphitic carbon nitride/reduced graphene oxide/layered MnO_2 (g-C_3N_4/rGO/MnO_2) ternary nanocomposite. Such unique architectures, which were the different nanosheets stacking with each other, could endow the material with excellent catalytic capacity. Furthermore, the as-prepared g-C_3N_4/rGO/MnO_2 nanocomposite showed excellent catalytic performance on thermal decomposition of ammonium perchlorate (AP), a key energetic oxidizer in composite solid propellants [21]. To be best of our knowledge, there are not any reports regarding the synthesis and application of sheet-on-sheet structured g-C_3N_4/rGO/MnO_2 nanocomposite till now.

2. Experimental

2.1. Synthesis of g-C_3N_4, g-C_3N_4/rGO and g-C_3N_4/rGO/MnO_2 Ternary Nanocomposite

Guanidine hydrochloride (GndCl) and potassium permanganate ($KMnO_4$) was purchased from Sinopharm Chemical Reagent Co., Ltd. (Beijing, China). Graphene oxide (thickness: 1~3 nm) was purchased from Nanjing XFNANO Materials Tech Co., Ltd. (Nanjing, China). All the chemicals were used without further purification.

Firstly, bulk g-C_3N_4 was synthesized by directly heating guanidine hydrochloride (GndCl) at 550 °C for 2 h in the tubular furnace under N_2 atmosphere at a heating rate of 3 $°C \cdot min^{-1}$ [9].

Secondly, g-C_3N_4/rGO binary composite was prepared by an in situ method that g-C_3N_4 was covalently coupled with rGO. Typically, 100 mg graphene oxide was dispersed in 100 mL distilled water under ultrasonic sound (300 W) for 1 h. Afterwards, 300 mg GndCl was added into the above GO suspension and the mixture was heated at 80 °C under stirring for 4 h. Then, the grey sponge-like precursor (labeled as GndCl/GO) was collected by freeze-drying. Finally, the as-prepared precursor was placed into a tube furnace and calcined at 550 °C (N_2 atmosphere) for 5 h at a heating rate of 3 °C·min^{-1} to obtain the binary composite labeled as g-C_3N_4/rGO (1:X). the X was the mass radio of the GndCl and GO.

Thirdly, the g-C_3N_4/rGO/MnO_2 ternary nanocomposite was prepared by adding 20 mg $KMnO_4$ into 100 mL g-C_3N_4/rGO (1:3) binary composite suspension (0.4 mg/mL) and stirred at 80 °C for 2 days. The final production was collected by filtrating, washing and freeze-drying.

For comparison, pure MnO_2 nanosheets without g-C_3N_4 and rGO were also obtained using the same method under the same condition. In detail, excess $KMnO_4$ was added to the rGO suspension and stirred at 80 °C for 2 days. The resulted sample was collected by washing with deionized water and freeze-drying.

2.2. Characterization

The X-ray diffraction (XRD) patterns at wide (10–80° in 2θ) angles were collected using a Bruker D8 Advanced X-ray diffractometer (Bruker, Billerica, MA, USA) with Cu Kα irradiation (λ = 0.15406 nm). Fourier transform infrared (FT-IR) spectra of samples were recorded on Bruker Tensor 27 spectrometer (Bruker, Billerica, MA, USA). Raman spectrometer was conducted using a Laser Confocal inVia Raman Microspectrometer (Renishaw, UK) equipped with a 514 nm Ar ion solid excitation laser. The small peaks centered at 1120 cm^{-1} in all the Raman spectrum curve were assigned to the interference of fluorescence. X-ray photoelectron spectra (XPS) was performed using a Thermo Fisher ESCALAB250Xi instrument (Thermo Fisher, Waltham, MA, USA) with Al Kα radiation as the exciting source. The results obtained in the XPS analysis were corrected by referencing the C1s line to 284.8 eV. Transmission electron microscopy (TEM) images were obtained using a JEM-2100 microscope (JEOL, Tokyo, Japan) with an accelerating voltage of 100 kV. Energy-dispersive X-ray maps from the Scanning Transmission Electron Microscope were recorded using an FEI-Tecnai G2 F30 S-TWIN TEM (FEI, Hillsboro, OR, USA) operated at 200 kV. BET surface areas were obtained from 77 K N_2 adsorption-desorption isotherms using a MICROMERITICS ASAP2020 surface area and porosimetry analyzer (Micromeritics, Norcross, GA, USA).

2.3. Catalytic Activity Measurement

To research on the catalytic performance of the as-prepared materials on the thermal decomposition of AP, a sample of AP mixed with g-C_3N_4, g-C_3N_4/rGO, MnO_2 and g-C_3N_4/rGO/MnO_2 were prepared, respectively.

Preparation of sample for catalytic research: 0.02 g of g-C_3N_4, g-C_3N_4/rGO, MnO_2 and g-C_3N_4/rGO/MnO_2 were mixed with 0.98 g of AP in ethanol at room temperature, respectively, stirred for 1 h and then dried at 60 °C for 1 h.

The resulting sample was determined by DSC (American TA Instrument SDT Q600, American TA Instrument, New Castle, DE, USA) and TG (Beijing Hengjiu Instrumnet HTG-1, Beijing Hengjiu Instrumnet, Beijing, China) at a heating rate of 10 °C·min^{-1} over the range of 100–500 °C under N_2 atmosphere.

3. Result and Discussion

The overall synthetic procedure of the g-C_3N_4/rGO/MnO_2 ternary nanocomposite was illustrated in Scheme 1. First, covalently coupled g-C_3N_4/rGO binary nanocomposite was fabricated through the in situ pyrolysis of guanidinium chloride (GndCl) on the surface of GO at 550 °C under nitrogen. During this process, water-soluble GndCl was firstly reacted with the active epoxy groups of GO via a nucleopilic substitution reaction. Upon calcining above precursor (GO-GndCl) under 550 °C, g-C_3N_4 was in situ prepared via the polymerization of GndCl. Meanwhile, nitrogen-containing species were released, which led to the partial reduction of GO. Subsequently, the as-prepared g-C_3N_4/rGO binary nanocomposite was dispersed in $KMnO_4$ aqueous solution (80 °C) for two days. In this way, carbon atoms in the rGO framework would react with $KMnO_4$ to in situ form MnO_2 nanosheets via the partial depletion of rGO, which ultimately constructed g-C_3N_4/rGO/MnO_2 ternary nanocomposite.

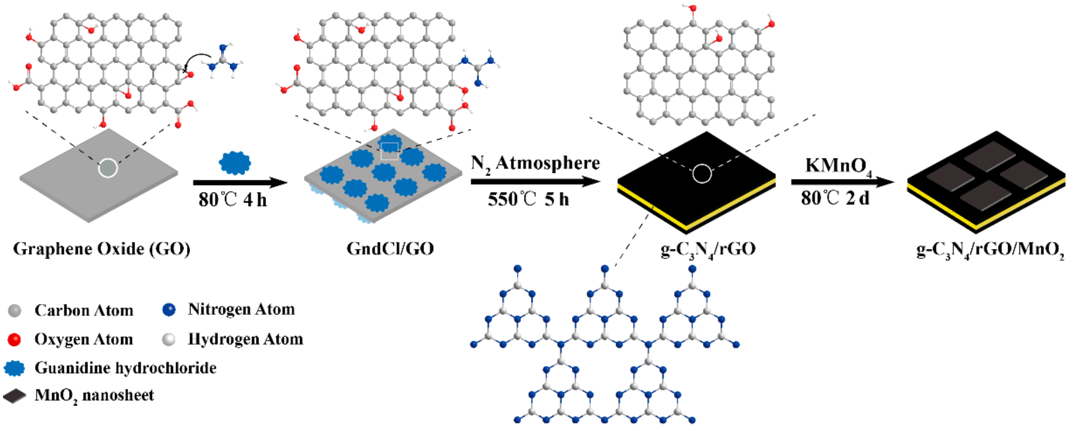

Scheme 1. Illustration of the synthetic method of the g-C_3N_4/rGO/MnO_2 ternary nanocomposite.

Figure 1 shows the FT-IR spectra of the GndCl, GndCl-GO and GO. Pure GO exhibited several absorption peaks in the range of 1000–2000 cm^{-1}: C–OH (1051 cm^{-1}), epoxide C–O–C (1221 cm^{-1}), aromatic C=C (1628 cm^{-1}) and C=O (1727 cm^{-1}). It could be clearly found that the epoxide C–O–C peak of GndCl-GO at 1221 cm^{-1} was almost disappeared, which was attribute to the ring-opening reaction between NH_2 (nucleophiles) and C–O–C group via an S_N2 mechanism [13], demonstrating that GndCl was successfully grafted onto the surface of GO.

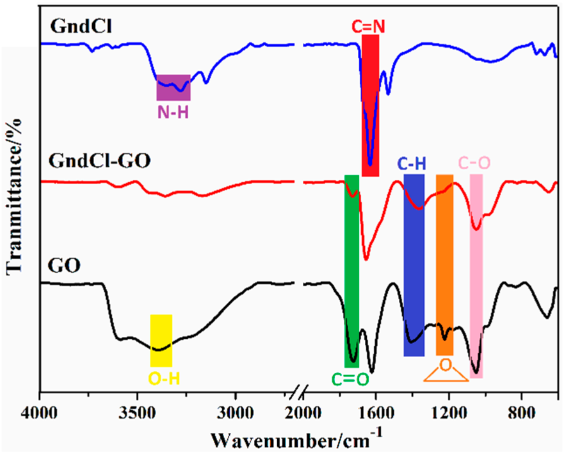

Figure 1. FT-IR spectra of GndCl, GO and GndCl-GO.

The as-prepared precursor (GO-GndCl) was then calcined to obtain the g-C_3N_4/rGO nanocomposite. Figure S1 showed the FT-IR curves of g-C_3N_4/rGO. It can be found that, apart from the absorption peaks belonging to g-C_3N_4, g-C_3N_4/rGO also exhibited an adsorption peak at 1558 cm^{-1}, which could be assigned to the stretching vibrations of the graphene nanosheets [22]. This further confirmed the thermal reduction of GO under pyrolysis reaction. The crystal structure of the g-C_3N_4/rGO was investigated by X-ray diffraction (XRD). As shown in Figure 2, rGO exhibited a broad diffraction peak at 25.0°, corresponding to the inter-layer space about 0.36 nm of (002) plane. g-C_3N_4 contained two distinct diffraction peaks located at about 13.2° and 27.4°, which could be indexed of the (100) and (002) planes of hexagonal g-C_3N_4 (JCPDS 87-1526) [23], corresponding to the inter-layer stacking of aromatic segments with a distance of 0.33 nm and the in-plane structural packing motif, respectively. For g-C_3N_4/rGO nanocomposite with various content of g-C_3N_4, they only exhibited one diffraction peak between 25.0° and 27.4°, indicating a medium inter-layer distance compared to pure g-C_3N_4 and rGO, respectively, which could be ascribed to the stagger inter-layer stacking of g-C_3N_4 and rGO nanosheet.

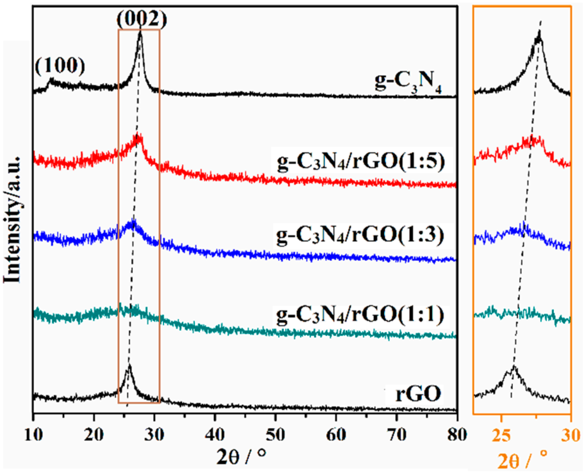

Figure 2. X-Ray Diffraction (XRD) diffraction pattern of g-C_3N_4, rGO, g-C_3N_4/rGO nanocomposite.

X-ray photoelectron spectroscopy (XPS) was used to further study the element composition and chemical state of g-C_3N_4/rGO nanocomposite. From the data list in Table 1, the O content of g-C_3N_4/rGO was 9.13 wt %, which was lower that of pure GO (38.63 wt %), reflecting the partial reduction of GO via deoxygenation. Meanwhile, the presence of the introduction of g-C_3N_4 which have no oxygen also contributed to a decrease of O content in the g-C_3N_4/rGO composite. As shown in Figure 3a, compared with pure GO, the spectrum of GndCl-GO contained not only C and O element but also N element. Besides, as shown in Table 2 and Figure 3b, compared with pure GO, the epoxy group content of GO-GndCl was much lower, whereas hydroxyl groups content was remarkably increased. All these further support that GndCl was grafted onto GO via ring opening reaction, producing a large number of hydroxyl groups. The C1s spectra of the g-C_3N_4/rGO (Figure 3c) could be de-convoluted into five peaks located at 284.8 eV (C=C), 285.7 eV (C–OH), 286.9 eV (C–O–C), 288.6 eV (–COOH) and 289.3 eV (C–N). Except for the peaks belonging to rGO, it also contained the peak corresponding to C–N, suggesting the successful construction of g-C_3N_4/rGO nanocomposite. The N1s spectra (Figure 3d) provided further information regarding the formation of g-C_3N_4/rGO. It could be fitted into different peaks located at 398.9 eV, 399.8 eV and 401.4 eV, which could be assigned to sp^2-hybridized pyridine nitrogen in triazine rings (C–N=C), tertiary nitrogen N–$(C)_3$ groups and amino function ($(C)_2$–N–H), respectively [24]. In addition, the peak at 405.1 eV was attributed to the charging effect of nitrogen-containing aromatic polymer [25], also reflecting the existence of g-C_3N_4 in the binary nanocomposite, which was in accordance with the C1s results discussed above.

Table 1. C, O and N content (at%/wt %) of the sample according to XPS analysis from Figure 3.

Samples	C	N	O	Cl
GO	67.93/61.37	/	32.07/38.63	/
GndCl/GO	36.04/27.05	21.37/18.71	33.06/33.08	9.53/21.16
g-C_3N_4/GO	59.54/55.14	33.07/35.73	7.39/9.13	/

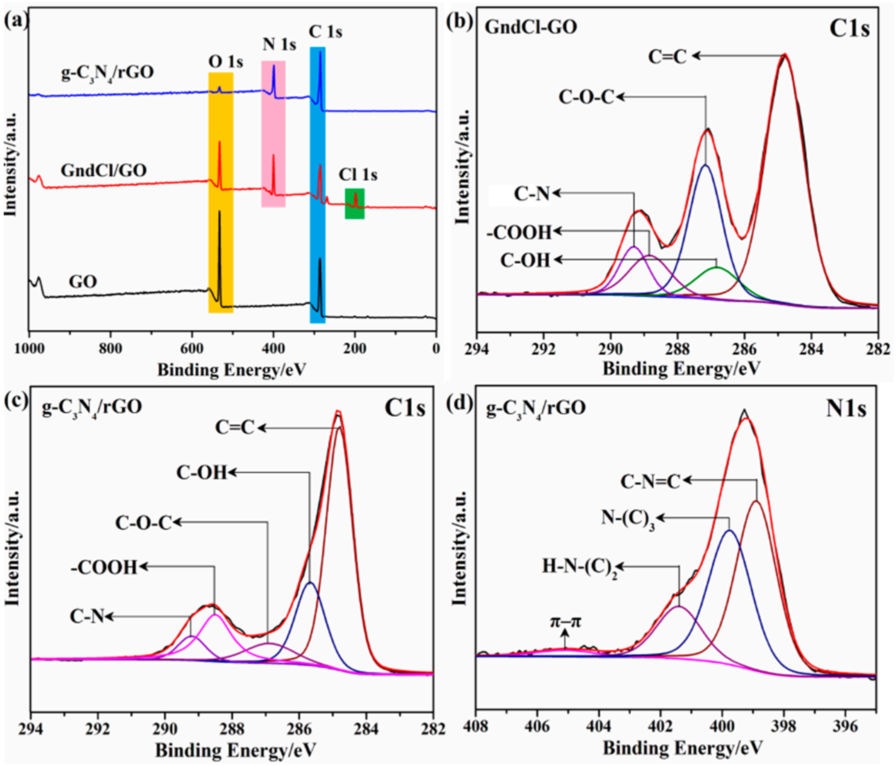

Figure 3. (**a**) XPS survey spectra of the GO, GndCl/GO and g-C_3N_4/rGO nanocomposite. (**b**) High resolution C 1s spectra of GndCl/GO precursor. High resolution C 1s (**c**) and N 1s (**d**) spectra of the g-C_3N_4/rGO nanocomposite.

Table 2. C species content (at%) of the sample according to XPS analysis from Figure 3.

Samples	C=C	N–C=N	C–O–C	C–OH	–COOH
GO	48.01	/	44.57	2.97	4.45
GndCl/GO	51.95	7.56	23.97	7.51	9.02
g-C_3N_4/GO	51.61	5.31	7.89	19.80	15.40

g-C_3N_4/rGO/MnO_2 ternary nanocomposite was synthesized via in situ formation of MnO_2 nanosheet onto the surface of g-C_3N_4/rGO through oxidation-reduction reaction. Figure 4a showed the XRD spectra of g-C_3N_4/rGO/MnO_2 nanocomposite, revealing the co-existence of g-C_3N_4, rGO and MnO_2 in the ternary nanocomposite. The strong peak at $2\theta = 12.0°$, could be indexed as (001) of MnO_2 nanosheet, indicating the layered hexagonal system, corresponding to a distance of 0.74 nm [26]. Meanwhile, the peak at 26.6° was assigned to inter-layer stagger stacking of the rGO and g-C_3N_4 nanosheet, which could be indexed as (002) plane with the distance of 0.34 nm [13]. In addition, the tiny peaks at 36.1° and 65.2° were indexed as (100) and (110) planes for the hexagonal 2D unit cell of MnO_2 [16], which was also the evidence of the formation of layered MnO_2 nanosheet. In order to further confirm the formation of g-C_3N_4/rGO/MnO_2 nanocomposite, samples were characterized by Raman spectroscopy (Figure 4b). The appearance of small peak in the range of 550–700 cm^{-1}, which could be assigned to Mn–O lattice vibrations [27], as well as the decrease of the D and G bands in the ternary nanocomposite demonstrate the yield of MnO_2 nanosheet via partial depletion of rGO. The results of the XRD and Raman were in good agreement with FT-IR analysis (Figure S2).

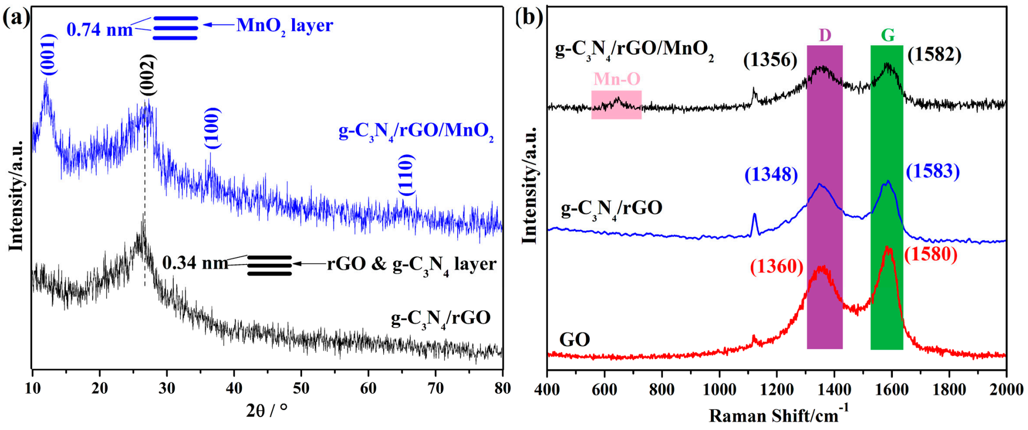

Figure 4. (**a**) XRD diffraction pattern of g-C_3N_4/rGO/MnO_2 ternary nanocomposite. (**b**) Raman spectra of GO, g-C_3N_4/rGO and g-C_3N_4/rGO/MnO_2 ternary nanocomposite.

Figure 5a was the XPS survey spectra of g-C_3N_4/rGO/MnO_2, which simultaneously contains C, N, O, Mn element, indicating the incorporation of Mn element into the framework of g-C_3N_4/rGO/MnO_2. Furthermore, the separation of spin-energy between Mn $2p^{1/2}$ (654.4 eV) and $2p^{3/2}$ (642.4 eV) was 11.8 eV, confirming the existence of MnO_2 [26] (Figure 5b). Figure 5c,d shows the high resolution C1s and N1s spectra of the g-C_3N_4/rGO/MnO_2, respectively. Both the C 1s peak and N 1s peak could be fitted in four peaks, which were in accordance with the XPS analysis of g-C_3N_4/rGO nanocomposite, reflecting the existence of g-C_3N_4 and rGO in the ternary nanocomposite. However, being different from g-C_3N_4/rGO, the O1s spectra of g-C_3N_4/rGO/MnO_2 could be de-convoluted into five peaks located at 529.9 eV, 531.4 eV, 533.0 eV and 534.2 eV (Figure 5e). The peaks at 529.9 eV and 531.4 eV were ascribed to the lattice of [MnO_6] octahedra and the adsorbed oxygen in the presence of water molecular (Mn–OH) [16], respectively, which belong to MnO_2 nanosheet. Besides, the peak at 533.0 eV was the typical C–O signal [12], which could be attributed to the presence of rGO.

Transmission electron microscopy (TEM) study showed that pure GO exhibited layered structure with large aspect ratio (Figure 6a). Besides, as shown in Figure 6b, the as-prepared g-C_3N_4/rGO nanocomposite consisted of many pores, which could be attributed to gas removal (NH_3, HCl) during pyrolysis process. Meanwhile, it could be clearly seen that g-C_3N_4/rGO showed a 2D layered structure with chiffon-like ripples and wrinkles. For g-C_3N_4/rGO/MnO_2 nanocomposite (Figure 6c), the surface of g-C_3N_4/rGO was uniformly covered with MnO_2 nanosheet with a sheet-on-sheet structure. Additionally, Figure 6e showed the enlarged TEM image of g-C_3N_4/rGO/MnO_2. Notably, there was an intimate interfacial contact between MnO_2, g-C_3N_4 and rGO nanosheet. To further illustrate the element distribution of the ternary nanocomposite, scanning transmission electron microscopy (STEM) experiment was carried out. Figure 6d was the STEM images of g-C_3N_4/rGO/MnO_2 in dark field. Figure 6d1–d6 showed the element mapping of C, N, Mn and O, displaying the good distribution of MnO_2 nanosheet on the interface of g-C_3N_4/rGO. Meanwhile, the energy dispersive X-Ray analysis (EDX) indicated the simultaneous presence of C, N, Mn and O (Figure 6f), which was in accordance with the analysis of element mapping. Figure 6g and h depicted the HRTEM images of g-C_3N_4/rGO/MnO_2. As shown in Figure 6g, the lateral view showed the layered structure of the MnO_2 nanosheet, giving a 0.74 nm lattice spacing of the (001) planes of MnO_2. Besides, the HRTEM image in Figure 6h indicated a 0.34 nm basal spacing, corresponding to the (100) planes of g-C_3N_4/rGO nanocomposite. The TEM morphology characterization indicated that the g-C_3N_4/rGO/MnO_2 were layer-structured nanosheets with large width-to-thickness ratio.

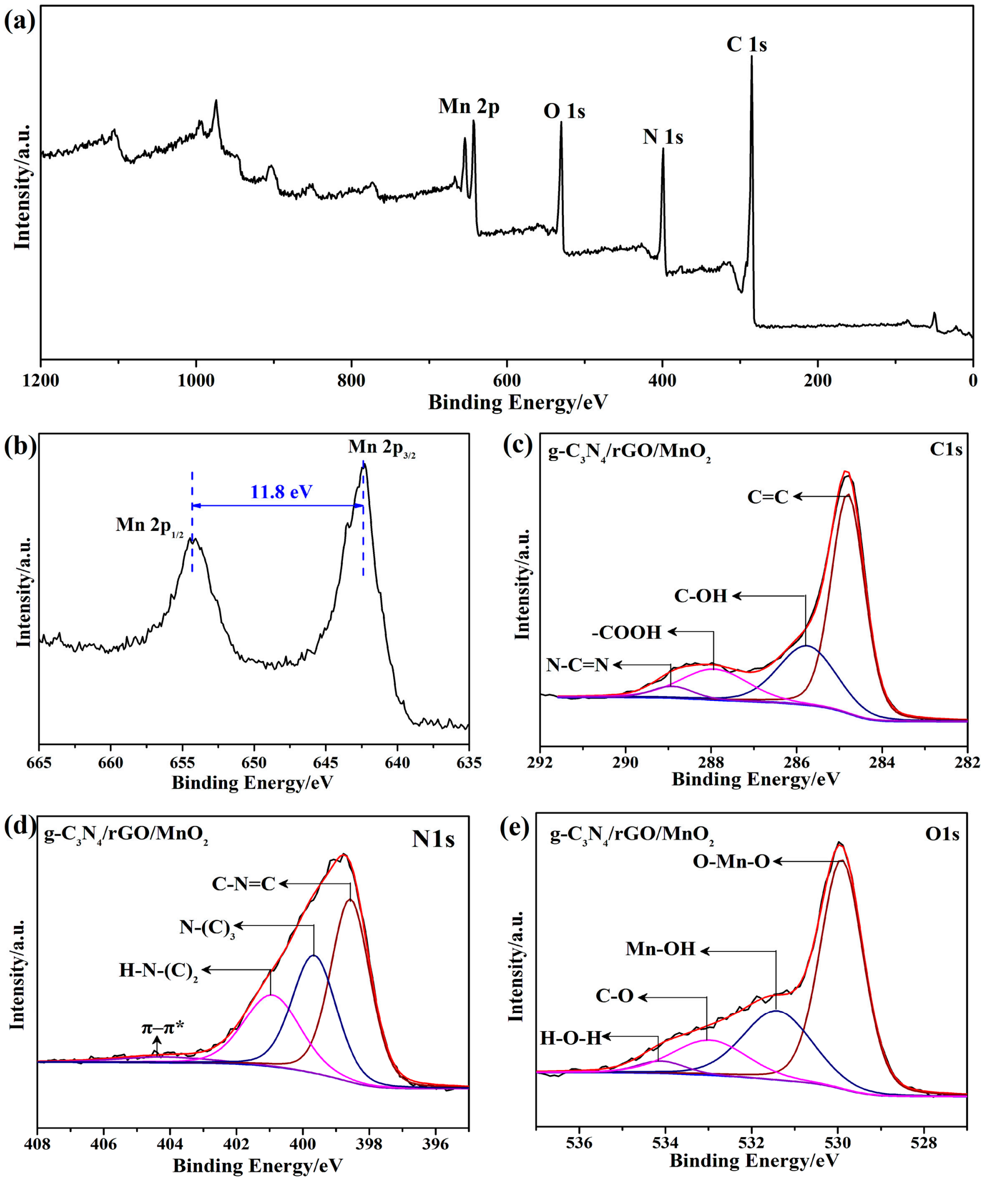

Figure 5. XPS spectra of the g-C_3N_4/rGO/MnO_2 ternary nanocomposite: (**a**) full scan, (**b**) high resolution Mn 2p, (**c**) high resolution C 1s, (**d**) high resolution N 1s, (**e**) high resolution O 1s.

The catalytic performance of g-C_3N_4/rGO/MnO_2 ternary nanocomposite on thermal decomposition of ammonium perchlorate (AP) was investigated by DSC and TG and the results were illustrated in Figure 7. Figure 7a presented the DSC curves of AP in the absence and presence of 2 wt % g-C_3N_4, g-C_3N_4/rGO, MnO_2 and g-C_3N_4/rGO/MnO_2 catalyst, respectively. As shown, the thermal decomposition of pure AP contained two exothermic peaks: the high-temperature decomposition (HTD) centered at 309.5 °C and the low-temperature decomposition (LTD) centered at 432.3 °C. Besides, the endothermic peak at 248.3 °C was assigned to the crystal transformation process of AP [23]. The addition of different catalyst resulted in significant changes of the both high-temperature decomposition peak and low-temperature decomposition peak, whereas did not affect the crystal transformation temperature. Indeed, upon treated with 2 wt % pure g-C_3N_4 catalyst, the HTD peak of AP was decreased by 41.6 °C with the exothermic quantity of 951.2 J/g, which was similar to the previous reports [21], indicating the g-C_3N_4 was a promising catalyst for AP's decomposition. Compared with the pure g-C_3N_4 catalyst, g-C_3N_4/rGO exhibited better catalytic performance than g-C_3N_4 alone and the HTD peak of AP could be decreased by 67.5 °C. This was attributed to the good conductivity of rGO, which could effectively accelerate the transfer of electron during the catalytic reaction [28]. For comparison, we also utilized rGO as templet to prepare pure MnO_2 catalyst. As shown in DSC curves (Figure 7a), MnO_2 also exhibited good catalytic ability on thermal decomposition of AP and the corresponding HTD peak was decreased by 105.2 °C with the exothermic quantity of 1423.0 J/g in the presence of 2 wt % MnO_2. Notably, when AP was mixed with 2 wt % g-C_3N_4/rGO/MnO_2 ternary nanocomposite, the HTD peak was remarkably decreased by 125.5 °C. Meanwhile, the exothermic heat of AP in the presence of this ternary catalyst was the highest comparing with other lines shown in Figure 7a, which was up to 1669.1 J/g (Figure 7b), demonstrating the promising synergistic catalysis.

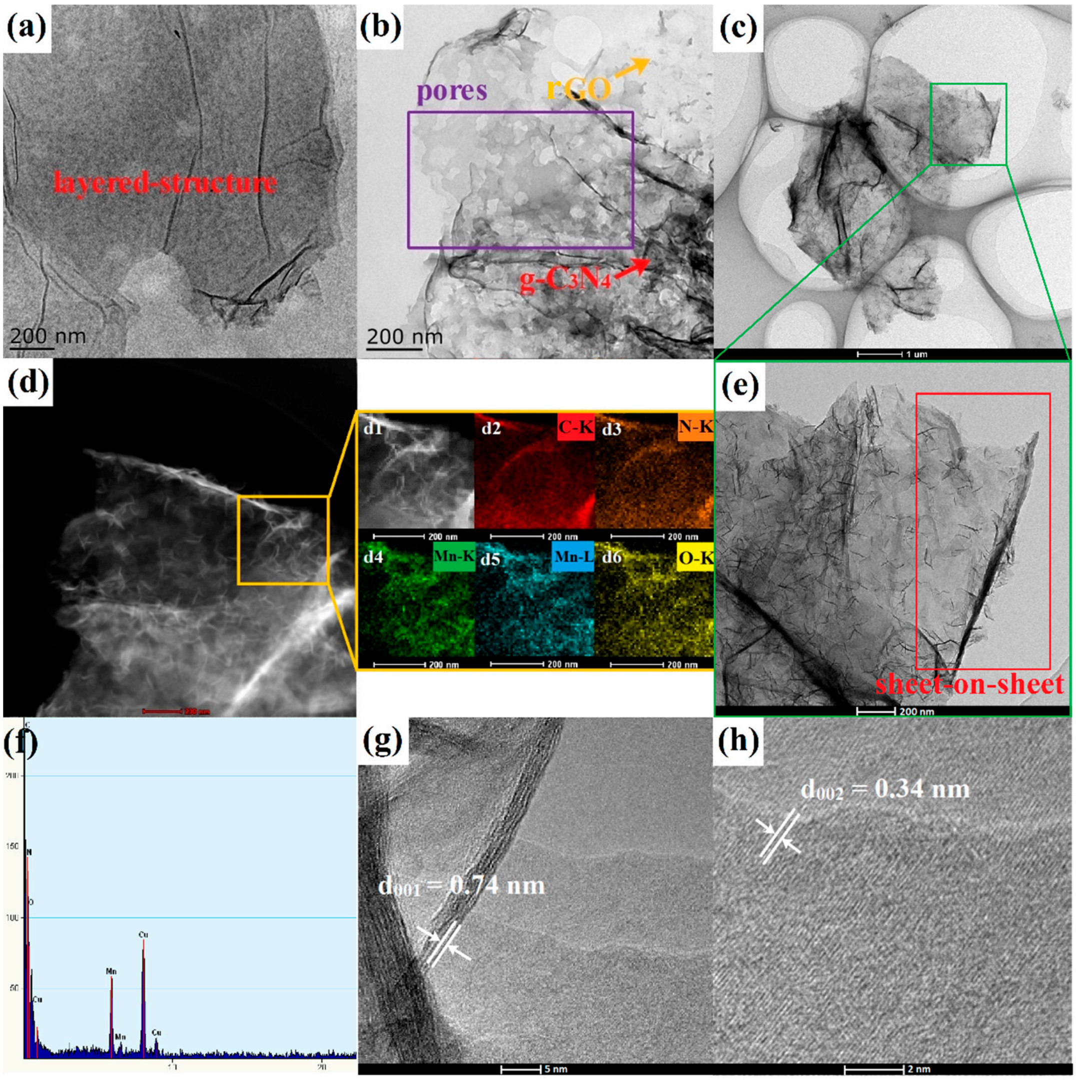

Figure 6. TEM images of (**a**) GO, (**b**) g-C_3N_4/rGO and (**c**,**e**) g-C_3N_4/rGO/MnO_2 ternary nanocomposite. (**d**) elemental mappings, (**f**) EDS spectrum, (**g**,**h**) HRTEM images of the g-C_3N_4/rGO/MnO_2 ternary nanocomposite. (inset images, corresponding height).

Figure 7c,d was the TG and DTG curves of the as-prepared samples, respectively. As displayed in Figure 7c, upon addition of g-C_3N_4 and g-C_3N_4/rGO binary nanocomposite as catalyst, respectively, the TG lines showed two weight loss steps from 100 °C to 500 °C, which was similar to the weight loss steps of pure AP in the absence of catalyst [29]. However, the two weight loss steps of AP were converted into a single step rapid decomposition process and the ending weight-loss decomposition temperature decreased in the presence of MnO_2 and g-C_3N_4/rGO/MnO_2 ternary nanocomposite, respectively, indicating that MnO_2 and g-C_3N_4/rGO/MnO_2 exhibited better catalytic performance than g-C_3N_4 and g-C_3N_4/rGO. Furthermore, in order to obviously distinguish the catalytic ability of MnO_2 and g-C_3N_4/rGO/MnO_2, we took the derivation of TG lines and the corresponding DTG curve was shown in Figure 7d. Specifically, the weight-loss decomposition temperature of AP in the presence 2 wt % MnO_2 decreased by 122.4 °C, which was in accordance with the DSC analysis. However, when treated with 2 wt % g-C_3N_4/rGO/MnO_2 ternary catalyst, the weight-loss decomposition temperature of AP was decreased by 142.5 °C, which was much higher than that of pure g-C_3N_4, g-C_3N_4/rGO and MnO_2, separately. All these further suggested that the catalytic capacity of the ternary nanocomposite was remarkably enhanced via the synergistic effect of g-C_3N_4, rGO and MnO_2. Based on DSC and TG analysis, we concluded that the as-prepared sheet-on-sheet structured 2D ternary g-C_3N_4/rGO/MnO_2 nanocomposite exhibited excellent catalytic capacity on thermal decomposition of AP, which could be used as a promising catalyst for composite propellants in the future.

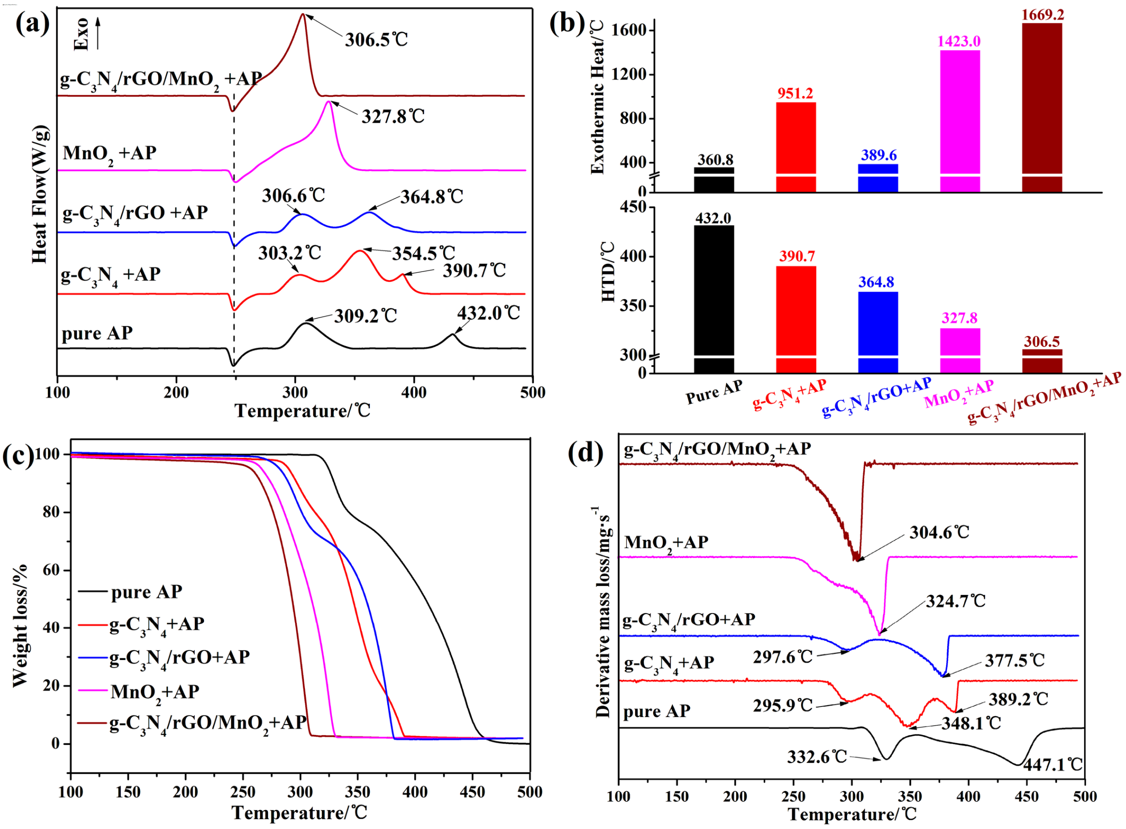

Figure 7. (**a**) DSC curves of AP in the absence and presence of catalysts. (**b**) histogram of the corresponding high decomposition temperature (HTD) and exothermic heat in Figure 7a. (**c**) TG and (**d**) DTG curves of AP in the absence and presence of catalysts. (the mass radio of catalyst to AP is 1:49).

Why did the ternary g-C_3N_4/rGO/MnO_2 exhibit excellent catalytic capacity than single g-C_3N_4 and MnO_2 on thermal decomposition of AP? A previous study had demonstrated that the thermal decomposition process of AP consisted of two stages: low-temperature decomposition (LTD) process and high-temperature decomposition (HTD) process [30]. During the LTD process, a proton (H^+) in AP transferred from the cation NH_4^+ to the anion ClO_4^-, forming NH_3 and $HClO_4$. After that, the generated $HClO_4$ molecules decomposed rapidly and subsequently reacted with NH_3. During HTD process, the generated NH_3 and $HClO_4$ NH_3 in LTD process was completely oxidized by $HClO_4$ in the gas phase.

Recently, He's group demonstrated that g-C_3N_4 significantly affected the LTD process of AP [31]. In general, g-C_3N_4 possess a unique structure which was consisted of tri-s-triazine units connected by planar amino groups, which could be regarded as a Lewis base. During LTD process, the generated $HClO_4$ would be firmly absorbed on g-C_3N_4 by the Lewis acid-base interaction, leading to the separation of $HClO_4$ from the pores of AP. This was benefit to the proton transfer from NH_4^+ to ClO_4^-, accelerating the the decomposition process of AP [21].

Additionally, MnO_2 was also a fantastic catalyst for AP's thermal decomposition, confirmed by the DSC and TG data listed in Figure 7. As demonstrated by the previous literature, there were many lattice defects in the MnO_2, in which existed large number of positive holes (h^+) and electrons (e^-) [29]. During the thermal decomposition process, the e^- was released and then reacted with $HClO_4$ molecular to generate the superoxide radical anion $\cdot O_2^-$. Due to the power oxidation of the $\cdot O_2^-$ and h^+, the NH_3 would be further depleted to generate H_2O, NO_2 and N_2O [32].

Reduced graphene oxide (rGO) was an excellent conductor, which could effectively accelerate the transfer of electron (e^-), resulting in the faster decomposition of generated $HClO_4$ molecular during the catalytic reaction [28]. Besides, the unique sheet-on-sheet structure was also beneficial for the acceleration of the transfer of e^- between different layers. In brief, by combination of the function of g-C_3N_4, rGO and MnO_2, the ternary g-C_3N_4/rGO/MnO_2 would promote the thermal decomposition process of AP.

4. Conclusions

In summary, a sheet-on-sheet structured 2D ternary nanocomposite (g-C_3N_4/rGO/MnO_2) was successfully constructed via a two-step approach. In this procedure, FT-IR, XRD, Raman as well as the XPS were employed to investigate the formation process of the ternary nanocomposite. In general, GndCl was firstly grafted onto the interface of GO by ring-opening reaction to form GO-GndCl precursor and then the precursor was calcined, simultaneously leading to the formation of g-C_3N_4 and the reduction of GO, followed by the formation of covalently coupled g-C_3N_4/rGO nanocomposite. Secondly, layered MnO_2 nanosheets were in situ formed onto the surface of g-C_3N_4/rGO via a facile redox method, constructing sheet-on-sheet structured g-C_3N_4/rGO/MnO_2 ternary nanocomposite. The special layer-by-layer morphology ensured the excellent catalytic performance on thermal decomposition of AP. Upon addition of 2 wt % g-C_3N_4/rGO/MnO_2 ternary catalyst, the thermal decomposition temperature of AP was decreased by 142.5 °C, which was higher than that of pure g-C_3N_4, g-C_3N_4/rGO and MnO_2, respectively, demonstrating synergistic catalysis. Moreover, the fascinating structure of this g-C_3N_4/rGO/MnO_2 ternary nanocomposite could widely expand its application in battery anode, supercapacitors, water oxidation and oxygen reduction, fluorescence sensor and so on.

Supplementary Materials: The following are available online at http://www.mdpi.com/2079-4991/7/12/450/s1, Figure S1: FT-IR curves of the g-C_3N_4/rGO nanocomposite, Figure S2: FT-IR spectrum of the g-C_3N_4/rGO/MnO_2 Ternary Nanocomposite.

Acknowledgments: This work was supported by the Science Foundation of Nanjing Institute of Technology (ZKJ201402) and (ZKJ201501), the natural science foundation of Jiangsu Province (BK20160773), the National Natural Science Foundation of China (NSFC 21603102), the Extra-curricular Academic Scientific Research Fund of Nanjing University of Science and Technology and Undergraduate Research Training Millions Talents' Plan (2017) and the Priority Academic Program Development of Jiangsu Higher Education Institutions (PAPD).

Author Contributions: All the authors have been collaborating with each other to obtain a high-quality research work. L.T. and J.X. conceived and designed the experiments; D.L. and Y.C. performed the preparation experiments; B.K. analyzed the XRD and XPS data; W.J. and F.W. contributed the microstructure characterization of samples in STEM and HRTEM; J.X. and D.L. performed the catalytic experiments about the AP's decomposition. L.T. wrote the paper and F.L. contributed the revision of the paper.

Conflicts of Interest: The authors declare no conflict of interest.

References

1. Lu, Q.P.; Yu, Y.F.; Ma, Q.L.; Chen, B.; Zhang, H. 2D transition-metal-dichalcogenide-nanosheet-based composites for photocatalytic and electrocatalytic hydrogen evolution reactions. *Adv. Mater.* **2016**, *28*, 1917–1933. [CrossRef] [PubMed]
2. Ping, J.F.; Fan, Z.X.; Sindoro, M.; Ying, Y.B.; Zhang, H. Nanosheet sensors: Recent advances in sensing applications of two-Dimensional transition metal dichalcogenide nanosheets and their composites. *Adv. Funct. Mater.* **2017**, *27*. [CrossRef]
3. Ding, J.B.; Zhou, Y.; Li, Y.G.; Guo, S.J.; Huang, X.Q. MoS_2 nanosheet assembling superstructure with a three-dimensional ion accessible site: A new class of bifunctional materials for batteries and electrocatalysis. *Chem. Mater.* **2016**, *28*, 2074–2080. [CrossRef]
4. Kim, K.S.; Zhao, Y.; Jang, H.; Lee, S.Y.; Kim, J.M.; Kim, K.S.; Ahn, J.H.; Kim, P.; Choi, J.Y.; Hong, B.H. Large-scale pattern growth of graphene films for stretchable transparent electrodes. *Nature* **2009**, *457*, 706–710. [CrossRef] [PubMed]
5. Lee, C.G.; Wei, X.D.; Kysar, J.W.; Hone, J. Measurement of the elastic properties and intrinsic strength of monolayer graphene. *Science* **2008**, *321*, 385–388. [CrossRef] [PubMed]
6. Dreyer, D.R.; Park, S.; Bielawski, C.W.; Ruoff, R.S. The chemistry of graphene oxide. *Chem. Soc. Rev.* **2010**, *39*, 228–240. [CrossRef] [PubMed]
7. Qu, B.H.; Ma, C.Z.; Ji, G.; Xu, C.H.; Xu, J.; Meng, Y.S.; Wang, T.H.; Lee, J.Y. Layered SnS_2-reduced graphene oxide composite—A high-capacity, high-rate and long-cycle life sodium-ion battery anode material. *Adv. Mater.* **2014**, *26*, 3854–3859. [CrossRef] [PubMed]
8. Yang, J.; Voiry, D.; Ahn, S.J.; Kang, D.; Kim, A.Y.; Chhowalla, M.; Shin, H.S. Two-Dimensional hybrid nanosheets of tungsten disulfide and reduced graphene oxide as catalysts for enhanced hydrogen evolution. *Angew. Chem. Int. Ed.* **2013**, *52*, 13751–13754. [CrossRef] [PubMed]
9. Wang, X.C.; Maeda, K.; Thomas, A.; Takanabe, K.; Xin, G.; Carlsson, J.M.; Domen, K.; Antonietti, M. A metal-free polymeric photocatalyst for hydrogen production from water under visible light. *Nat. Mater.* **2009**, *8*, 76–80. [CrossRef] [PubMed]
10. Tian, J.Q.; Ning, R.; Liu, Q.; Asiri, A.M.; Al-Youbi, A.O.; Sun, X.P. Three-dimensional porous supramolecular architecture from ultrathin g-C_3N_4 nanosheets and reduced graphene oxide: Solution self-assembly construction and application as a highly efficient metal-free electrocatalyst for oxygen reduction reaction. *ACS Appl. Mater. Interface* **2014**, *6*, 1011–1017. [CrossRef] [PubMed]
11. Liao, G.Z.; Chen, S.; Quan, X.; Yu, H.T.; Zhao, H.M. Graphene oxide modified g-C_3N_4 hybrid with enhanced photocatalytic capability under visible light irradiation. *J. Mater. Chem.* **2012**, *22*, 2721–2726. [CrossRef]
12. Li, Y.B.; Zhang, H.M.; Liu, P.R.; Wang, D.; Li, Y.; Zhao, H.J. Cross-Linked g-C_3N_4/rGO nanocomposites with tunable band structure and enhanced visible light photocatalytic activity. *Small* **2013**, *9*, 3336–3344. [CrossRef] [PubMed]
13. Fu, Y.S.; Zhu, J.W.; Hu, C.; Wu, X.D.; Wang, X. Covalently coupled hybrid of graphitic carbon nitride with reduced graphene oxide as a superior performance lithium-ion battery anode. *Nanoscale* **2014**, *6*, 12555–12564. [CrossRef] [PubMed]
14. Ong, W.J.; Tan, L.L.; Chai, S.P.; Yong, S.T. Graphene oxide as a structure-directing agent for the two-dimensional interface engineering of sandwich-like graphene-g-C_3N_4 hybrid nanostructures with enhanced visible-light photoreduction of CO_2 to methane. *Chem. Commun.* **2015**, *51*, 858–861. [CrossRef] [PubMed]
15. Hou, Y.; Wen, Z.H.; Cui, S.M.; Guo, X.R.; Chen, J.H. Constructing 2D porous graphitic C_3N_4 nanosheets/nitrogen-doped graphene/layered MoS_2 ternary nanojunction with enhanced photoelectrochemical activity. *Adv. Mater.* **2013**, *25*, 6291–6297. [CrossRef] [PubMed]
16. Zhao, G.X.; Li, J.X.; Jiang, L.; Dong, H.L.; Wang, X.K.; Hu, W.P. Synthesizing MnO_2 nanosheets from graphene oxide templates for high performance pseudosupercapacitors. *Chem. Sci.* **2012**, *3*, 433–437. [CrossRef]
17. Deng, R.R.; Xie, X.J.; Vendrell, M.; Chang, Y.T.; Liu, X.G. Intracellular glutathione detection using MnO_2-nanosheet-modified upconversion nanoparticles. *J. Am. Chem. Soc.* **2011**, *133*, 20168–20171. [CrossRef] [PubMed]

18. Zhao, Z.L.; Fan, H.H.; Zhou, G.F.; Bai, H.R.; Liang, H.; Wang, R.W.; Zhang, X.B.; Tan, W.H. Activatable fluorescence/MRI bimodal platform for tumor cell imaging via MnO_2 nanosheet-aptamer nanoprobe. *J. Am. Chem. Soc.* **2014**, *136*, 11220–11223. [CrossRef] [PubMed]
19. Zhang, X.L.; Zheng, C.; Guo, S.S.; Li, J.; Yang, H.H.; Chen, G.N. Turn-on fluorescence sensor for intracellular imaging of glutathione using g-C_3N_4 nanosheet-MnO_2 sandwich nanocomposite. *Anal. Chem.* **2014**, *86*, 3426–3434. [CrossRef] [PubMed]
20. Zhang, L.S.; Lian, J.S.; Wu, L.Y.; Duan, Z.R.; Jiang, J.; Zhao, L. Synthesis of a thin-layer MnO_2 nanosheet-coated Fe_3O_4 nanocomposite as a magnetically separable photocatalyst. *Langmuir* **2014**, *30*, 7006–7013. [CrossRef] [PubMed]
21. Xu, J.H.; Li, S.Y.; Tan, L.H.; Kou, B. Enhanced catalytic activity of mesoporous graphitic carbon nitride on thermal decomposition of ammonium perchlorate via copper oxide modification. *Mater. Res. Bull.* **2017**, *93*, 352–360. [CrossRef]
22. Xiang, Q.J.; Yu, J.G.; Jaroniec, M. Preparation and enhanced visible-light photocatalytic H_2-production activity of graphene/C_3N_4 composites. *J. Phys. Chem. C* **2011**, *115*, 7355–7363. [CrossRef]
23. Tan, L.H.; Xu, J.H.; Zhang, X.J.; Hang, Z.S.; Jia, Y.Q.; Wang, S.B. Synthesis of g-C_3N_4/CeO_2 nanocomposites with improved catalytic activity on the thermal decomposition of ammonium perchlorate. *Appl. Surf. Sci.* **2015**, *356*, 447–453. [CrossRef]
24. Jian, X.; Liu, X.; Yang, H.M.; Li, J.G.; Song, X.L.; Dai, H.Y.; Liang, Z.H. Construction of carbon quantum dots/proton-functionalized graphitic carbon nitride nanocomposite via electrostatic self-assembly strategy and its application. *Appl. Surf. Sci.* **2016**, *370*, 514–521. [CrossRef]
25. Liu, Q.; Zhang, J.Y. Graphene supported Co-g-C_3N_4 as a novel metal-macrocyclic electrocatalyst for the oxygen reduction reaction in fuel cells. *Langmuir* **2013**, *29*, 3821–3828. [CrossRef] [PubMed]
26. Yu, N.; Yin, H.; Zhang, W.; Liu, Y.; Tang, Z.Y.; Zhu, M.Q. High-Performance fiber-shaped all-solid-state asymmetric supercapacitors based on ultrathin MnO_2 nanosheet/carbon fiber cathodes for wearable electronics. *Adv. Energy Mater.* **2016**, *6*. [CrossRef]
27. Liu, Y.C.; Miao, X.F.; Fang, J.H.; Zhang, X.X.; Chen, S.J.; Li, W.; Feng, W.D.; Chen, Y.Q.; Wang, W.; Zhang, Y.L. Layered-MnO_2 nanosheet grown on nitrogen-doped graphene template as a composite cathode for flexible solid-state asymmetric supercapacitor. *ACS Appl. Mater. Interface* **2016**, *8*, 5251–5260. [CrossRef] [PubMed]
28. Li, N.; Geng, Z.F.; Cao, M.H.; Ren, L.; Zhao, X.Y.; Liu, B.; Tian, Y.; Hu, C.W. Well-dispersed ultrafine Mn_3O_4 nanoparticles on graphene as a promising catalyst for the thermal decomposition of ammonium perchlorate. *Carbon* **2013**, *54*, 124–132. [CrossRef]
29. Chen, L.J.; Zhu, D.Y. Effects of different phases of MnO_2 nanorods on the catalytic thermal decomposition of ammonium perchlorate. *Ceram. Int.* **2015**, *41*, 7054–7058. [CrossRef]
30. Jacobs, P.W.M.; Whitehead, H.M. Decomposition and combustion of ammonium perchlorate. *Chem. Rev.* **1969**, *69*, 551–590. [CrossRef]
31. Li, Q.; He, Y.; Peng, R.F. Graphitic carbon nitride (g-C_3N_4) as a metal-free catalyst for thermal decomposition of ammonium perchlorate. *RSC Adv.* **2015**, *5*, 24507–24512. [CrossRef]
32. Li, Q.; He, Y.; Peng, R.F. TeO_2 nanoparticle loaded graphitic carbon nitride hybrids: Their preparation and catalytic activities in the thermal decomposition of ammonium perchlorate. *Eur. J. Inorg. Chem.* **2015**, *24*, 4062–4067. [CrossRef]